Supplementary Information

Fast and stable NH₄⁺ storage in multielectron H-bonding-acceptor organic molecules for aqueous zinc batteries

Qi Huang,[a] Ting Shi,[b] Yang Qin,[d] Yaowei Jin,[e] Lu Huang,[g] Yaojie Sun,[a, f] Chengmin Hu,*[c] Ziyang Song*[b] and Fengxian Xie*[a, f]

[a]Institute for Electric Light Sources, School of Information Science and Technology, Fudan University, Shanghai 200438, P. R. China.

[b]Shanghai Key Lab of Chemical Assessment and Sustainability, School of Chemical Science and Engineering, Tongji University, Shanghai 200092, P. R. China.

[c]Department of Chemistry, State Key Laboratory of Molecular Engineering of Polymers, Shanghai Key Lab of Molecular Catalysis and Innovative Materials, Collaborative Innovation Center of Chemistry for Energy Materials, Fudan University, Shanghai 200438, P. R. China.

[d]Department of Mechanical Engineering, College of Engineering and Applied Science, University of Wisconsin Milwaukee, Milwaukee, WI, 53211, USA.

[e]Lingang Laboratory, Shanghai 200031, P. R. China.

[f]Shanghai Engineering Research Center for Artificial Intelligence and Integrated Energy System, Fudan University, Shanghai 200433, P. R. China.

[g]Department of Stomatology, Hangzhou Ninth People's Hospital, Hangzhou 311225, P. R. China.

*Corresponding Authors

E-mail: hucmin@fudan.edu.cn (C. Hu), 21310240@tongji.edu.cn (Z. Song), xiefengxian@fudan.edu.cn (F. Xie).

Table of Contents

Fig. S11 (a) Tested pH values and (b) ionic conductivities of two electrolytes. (c) GCD profile of DNPQ in two different electrolytes.

Fig. S12 Differential capacity profile.

Fig. S13 GCD profiles of (a) PQ and (b) DN cathodes in NH_4OTF electrolyte.

Fig. S14 Ragone plots of Zn||DNPQ batteries based on the mass loading of DNPQ in the cathode (5.1 mg cm^{-2}) using NH_4OTF and $Zn(OTF)_2$ electrolytes, respectively.

Fig. S15 (a) CV curves of DNPQ at 1−5 mV s^{-1}. (b) b values, and (c) capacitive contribution of Zn//DNPQ battery using NH_4OTF electrolyte.

Fig. S16 Capacity comparison of DNPQ with recently reported organics.

Fig. S17 (a, c) Voltage profiles and (b, d) Coulombic efficiency of Zn||stainless-steel mesh cell in NH_4OTF and $Zn(OTF)_2$ electrolyte.

Fig. S18 Electrochemical impedance spectroscopy of pristine and cycled DNPQ cathode.

Fig. S19 Spatial geometric sizes of (a) hydrated NH_4^+ ions and (b) hydrated Zn^{2+} ions.

Fig. S20 Relationship between Z' and $\omega^{-0.5}$ in the intermediate frequency and corresponding NH_4^+ diffusion coefficient.

Fig. S21 Electrochemical impedance spectra of Zn||DNPQ battery at different temperatures in (a) NH_4OTF and (b) $Zn(OTF)_2$ electrolytes, respectively. The equivalent circuits for fitting Nyquist plots of DNPQ cathode in (c) NH_4OTF and (d) $Zn(OTF)_2$ electrolytes, including the equivalent series resistance (R_s), the charge transfer resistance (R_{ct}), the contact angle element (CPE), and Warburg resistance (Z_w). (e) Estimated R_{ct} values.

Fig. S22 Solubility of three samples.

Fig. S23 (a) Solubility and (b) photographs of DNPQ in two electrolytes.

Fig. S24 NH_4^+ uptake energies of DNPQ with different sites.

Fig. S25 The established geometry model of DNPQ.

Table S1 Comparison of rate capacity, energy density and cycling performance of recently reported organic cathode materials for ZOBs in the literatures.

Section S1. Experimental Procedures

1.1 Material Synthesis.

4,4'-dinitrobipenyl (DN, AR, 99%), 9,10-phenanthraquinone (PQ, AR, 99%) and 2,7-dinitrophenanthrene-9,10-dione (DNPQ, AR, 99%) organic small molecule were purchased from Shanghai Titan Technology Exploration Platform.

1.2 Material Characterizations.

Field-emission scanning electron microscopy (SEM, Hitachi S-4800) were applied to observe the microstructure and geometries of as-purchased samples. X-ray diffraction (XRD) pattern was performed to monitor the structures of organic materials (Cu Kα radiation source). Fourier-transformed infrared spectrum (FT-IR) was analyzed through a Thermo Nicolet NEXUS spectrometer. The elemental mapping image was captured on a JEM-F200 instrument equipped with an energy diffraction system. The UV-vis spectrum characterization was performed on a JASCO V-750 in a range of 200~800 nm to investigate the structural stability of the pristine and cycled DNPQ electrode soaked with $Zn(OTF)_2$ and NH_4OTF electrolytes after 30 days. X-ray photoelectron spectrometer (XPS, AXIS Ultra DLD) was utilized to investigate the surface functionalities of the samples. For *ex-situ* spectroscopic investigation including FT-IR and XPS, DNPQ cathodes were collected by disassembling ZOBs at specific voltages during the discharging/charging process.

1.3 Electrochemical Measurements.

DNPQ (or DN, PQ), graphite and polytetrafluoroethylene (with a mass ratio of 7:2:1) was mixed and compressed into discs, then pressed onto stainless-steel mesh. Afterwards, the cathodes were dried at 80 °C for 12 h at a vacuum condition. The mass loading of DNPQ on the cathode is ~5.1 mg cm^{-2}.

DNPQ (or DN, PQ) cathode, aqueous $NH_4CF_3SO_3$ electrolyte (named as NH_4OTF, 3 mol L^{-1}), Zn metal anode (> 99.99%), and glass fiber separator were coupled into a 2032 coin-type cell to assemble ZOBs. For comparison, aqueous $Zn(OTF)_2$ electrolyte (3 mol L^{-1}) was also applied to fabricate ZOBs.

Galvanostatic charge/discharge (GCD) profiles and cycling stability of ZOBs were collected

on a LAND-CT3002A battery test system with a voltage range of 0.1−1.8 V. Cyclic voltammetry (CV) and electrochemical impedance spectroscopy (EIS) tests were performed on a CHI660E electrochemical workstation. The specific capacity (C_m, mAh g^{-1}) was calculated from GCD profiles based on the following equation:

$$C_m = \frac{I \times \Delta t}{m} \tag{Eq. S1}$$

where I, Δt and m represent the current density (A g^{-1}), discharging time (s) and mass loading of active materials in cathodes, respectively.

The gravimetric energy density (E, Wh kg^{-1}) and power density (P, W kg^{-1}) of ZOBs were calculated according to the following equations:

$$E = C_m \times \Delta V \tag{Eq. S2}$$

$$P = \frac{E}{1000 \times \Delta t} \tag{Eq. S3}$$

where ΔV refers to the voltage window. The electrochemical specific capacities and energy/power densities were calculated based on the mass loading of active materials in the cathode.

The ion transport resistivity (σ, Ω s$^{-0.5}$) and diffusion coefficient (D, cm^2 s^{-1}) were investigated by EIS spectra according to the following equations:

$$Z' = \sigma\omega^{-0.5} + R_s + R_{ct} \tag{Eq. S4}$$

And the ion diffusion coefficient (D, cm^2 s^{-1}) is calculated by equation as follows:

$$D = \frac{R^2 T^2}{2A^2 C^2 F^4 n^4 \sigma^2} \tag{Eq. S5}$$

where Z': real part of impedance (Ω); σ: diffusion resistance (Ω s$^{-0.5}$); ω: angle frequency (rad s^{-1}); R_s: ohmic resistance between the electrode and electrolyte (Ω); R_{ct}: charge transfer resistance (Ω); n: electron transfer numbers per molecule during electron reaction; D: ion diffusion coefficient (cm^2 s^{-1}); A: surface area of electrode (cm^2); R: gas constant (8.314 J mol^{-1} K^{-1}); T: Kelvin temperature (293.15 K); C: molar concentration of electrolyte (mol L^{-1}); F: Faraday constant (96485 C mol^{-1}).

Section S2. Calculation Methods

2.1 Density Functional Theory (DFT) Calculation.

Molecular Property Simulation. The theoretical calculations were performed using the Gaussian 16 suite of programs.[S1−S4] The structures of DNPQ and its derivatives (DN and PQ) were optimized at the B3LYP-D3/ def2-TZVP level of theory. The negative electrostatic potential (ESP) region (red color) implies the electrophilic property, while the positive ESP (blue color) represent the nucleophilic one. The localized orbital locator-π (LOL-π) calculation was performed via Multiwfn 3.8 programs. The molecular orbital energy levels, including the lowest unoccupied molecular orbital (LUMO) and the highest occupied molecular orbital (HOMO), and the charge population sum were analyzed at the B3LYP-D3 level of theory. The independent gradient model (IGMH) based on Hirshfeld partition was conducted for optimized DNPQ complex to investigate the weak interaction between DNPQ and NH_4^+ charge carriers. The color-filled gradient isosurface map intuitively exhibit the interaction area and corresponding strength.

Geometry Optimization and Charge Density Difference: All the DFT calculations were carried out using the Vienna Ab initio Simulation Package (VASP)[S5] with the projector augmented wave (PAW) method.[S6] The exchange-functional was treated using the generalized gradient approximation (GGA) with Perdew-Burke-Emzerhof (PBE)[S7] functional. The energy cutoff for the plane wave basis expansion was tuned to be 400 eV. Partial occupancies of the Kohn−Sham orbitals were permitted by the Gaussian smearing method and a width of 0.2 eV. The Brillourin zone was sampled with Monkhorst mesh of 1×1×1 for the optimization for all the structures. The self-consistent calculations apply a convergence energy threshold of 10^{-4} eV, and the force convergency was tuned to be 0.05 eV $Å^{-1}$. The charge density differences were simulated by VASPKIT code. To detailly dissect the bonding properties of NH_4^+ uptake on DNPQ skeleton and charge transfer nature between both, the charge density differences of NH_4^+ absorbed on as-built DNPQ model were simulated through subtracting the charge densities of NH_4^+ and DNPQ substrates from the corresponding complexes. The charge transfer level between NH_4^+ and DNPQ was calculated by a Bader charge analysis procedure.[S8]

$$\Delta\rho = \rho(NH_4^+/DNPQ) - \rho(DNPQ) - \rho(NH_4^+) \tag{Eq. S6}$$

Molecular Dynamics Simulation. A standard molecular mechanic's potential model was employed based on the following equation:

$$u(r^N) = \sum_{bonds} \frac{k_i}{2}(l_i - l_{i,0})^2 + \sum_{angles} \frac{k_i}{2}(\theta_i - \theta_{i,0})^2 + \sum_{torsions} \frac{V_n}{2}(1 + \cos(n\omega - \gamma))$$
$$+ \sum_{i=1}^{N} \sum_{j=i+1}^{N} \left(4\varepsilon_{ij} \left[\left(\frac{\sigma_{ij}}{r_{ij}} \right)^{12} - \left(\frac{\sigma_{ij}}{r_{ij}} \right)^{6} \right] + \frac{q_i q_j}{r_{ij}} \right) \tag{Eq. S7}$$

where the first three terms denote the bonded interactions, including the bond length, bond angle, and torsion interactions, and the last term represents non-bonded interactions, including Coulombic interactions and van der Waals (vdW). For different kinds of atoms, the Lorentz-Berthelot mix rules were adopted for Van der Waals interactions based on the following equation:

$$\sigma_{ij} = \frac{1}{2}(\sigma_{ii} + \sigma_{jj}); \quad \varepsilon_{ij} = (\varepsilon_{ii} * \varepsilon_{jj})^{1/2} \tag{Eq. S8}$$

According to the experimental concentration, the simulated system was constructed. The initial configurations of the systems were established by the Packmol software.[S9] The simulations were performed using GROMACS package (version 2024.2)[S10–S13] with the all-atom OPLS (optimized performance for liquid systems) force field.[S14] The simple point charge/extend (SPC/E) model was employed to depict water molecules.[S15] For each system, the steep descent method was used to minimize the system energy. Subsequently, molecular dynamics simulations were conducted for each system (50 ns) under NPT ensemble at 298 K and 1 atm. The bond lengths of other components were restricted by LINCS algorithm.[S16] The periodic boundary conditions were applied in all three directions. The V-rescale thermostat algorithm was applied to hold the temperature constant.[S17] The long-range electrostatic interactions was calculated using Particle mesh Ewald method.[S18] The model configuration was visualized using Visual Molecular Dynamics software.[S19]

Several structures were taken from the finial simulated structures. Then the single-point energies of complexes were calculated using the density functional theory (DFT) at the B3LYP/def2-TZVP level.[S20] The calculations were carried out by using the Gaussian 16 package, revision A. 03.[S1] The binding energy (ΔE) of the configuration was estimated by the following form:

$$\Delta E = E_{AB} - (E_A + E_B) \tag{Eq. S9}$$

where E_A, E_B and E_{AB} represent the energies of A (one water molecule), B (excluding fragment A), and the total energy, respectively. A negative value of ΔE signifies that the reaction process is exothermic, and a higher negative value corresponds to a stronger interaction, which means that the more heat released, the more stable the structure.

Finete Element Simulation (FES). FES were performed using a COMSOL Multiphysics software to reveal the NH_4^+ ion transport process in DNPQ.[S21, S22] A sheet model was established, which stands for the section geometric architecture of DNPQ. The NH_4^+ ion diffusion process within DNPQ can be simulated according to the following Poisson–Nernst–Planck equation:

$$\nabla \cdot \left(D\nabla c_i + \frac{Dz_ie}{k_BT}c_i\nabla V \right) = 0 \qquad \text{(Eq. S10)}$$

where $D, c, z, e, T,$ and k_B is the diffusion coefficient, ion concentration, ion valence, elementary charge, absolute temperature, and Boltzmann constant, respectively. The above equation is solved in a time-dependent state to realize a steady state. To guarantee high accuracy of simulation result, the densest conventional triangular meshes were used for all simulations on the surface. The MUMPS solver was used with a relative tolerance of 0.001. The volume fraction is normalized by the maximum volume fraction in the center of DNPQ model.

2.2 Optical Energy Gap.

The optical energy gaps (E_g, eV) of DNPQ, DN and PQ were estimated based on UV-Vis spectra according to the following equations:[S23]

$$\alpha \propto \frac{(hv - E_g)^{1/2}}{hv} \qquad \text{(Eq. S11)}$$

$$hv = 1280/\lambda \qquad \text{(Eq. S12)}$$

where α signifies the optical absorption coefficient, hv is the photon energy, λ denotes the wavelength. The unit of E_g is eV.

2.3 Electron Tunneling Distance.

The tunneling probability (TP) of electron at the organic/graphite interface is related to the tunneling distance (x) and the height of potential height (β):[S24]

$$TP \propto e^{-\beta x} \qquad \text{(Eq. S13)}$$

A lower distance signifies a stronger π-π interaction between organic materials and the graphite additive and a higher electron tunneling probability. β is almost constant for a defined organic moiety. Thus, reducing the tunneling distance is the most feasible route to boost the interfacial charge transfer kinetics for electrochemical charge storage.

2.4 Activation Energy.

The activation energy (E_a, eV) for the charge transfer process was estimated by the Arrhenius equation:[S25]

$$1/R_{ct} = A\exp(-E_a/RT) \tag{Eq. S14}$$

where R_{ct}, A, and R represent the charge transfer resistance (Ω), constant under a stable experimental condition, the gas constant (8.314 J mol^{-1} K^{-1}), respectively. Plotting $\ln(R_{ct}^{-1})$ vs. $1000/T$ and linear fitting gets E_a:

$$\ln(R_{ct}^{-1}) = -E_a/RT + k \tag{Eq. S15}$$

where k is a constant.

2.5 Capacitive Contribution.

The charge storage kinetics of Zn||DNPQ batteries were studied according to the following relationship:[S26]

$$i = kv^b \tag{Eq. S16}$$

where k and b are constants, i and v refer to current density and scan rate, respectively. When the power exponent b value is close to 0.5, it identifies a diffusion-controlled process, while a b-value of 1.0 suggests a surface-dominated redox reaction process.[S27]

The Dunn's method was used to analyze the capacitive contribution from the rapid surface redox capacitive process and the diffusion-limited process.

Quantitative capacitive contribution can be calculated according to the following equation:[S27]

$$i = k_1 v + k_2 v^{1/2} \tag{Eq. S17}$$

where k_1 and k_2 are constants, $k_1 v$ and $k_2 v^{1/2}$ are the current density contributed from fast-capacitive process and diffusion-controlled process, respectively. Dividing $v^{1/2}$ on both sides of the above

equation gets:

$$i/v^{1/2} = k_1 v^{1/2} + k_2 \qquad \text{(Eq. S18)}$$

Generally, $i/v^{1/2}$ and $v^{1/2}$ show a linear relationship, two capacity contributions can be separated by linear fitting. The slope belongs to k_1 and the y-intercept equals k_2. By repeating the above steps for other voltages and sweep rates, the respective capacity contribution from the surface-controlled process and a diffusion-controlled process can be quantitatively calculated.

2.6 Theoretical Capacity Calculation.

The theoretical capacity (C_m, mAh g^{-1}) of an organic cathode was calculated according to the following form:[S28]

$$C_m = \frac{n \times F}{3.6 \times M} \qquad \text{(Eq. S19)}$$

where F denotes a constant (96485 C mol^{-1}), M is the molar mass of an organic material (g mol^{-1}). For DNPQ cathode, when considering the molecular weight of 298 g mol^{-1} and four-electron transfer during redox process, the theoretical capacity was calculated to be 270 mAh g^{-1}. Analogously, the theoretical capacity of DN and PQ were 220 and 129 mAh g^{-1}, respectively.

Section S3. Supplementary Characterizations
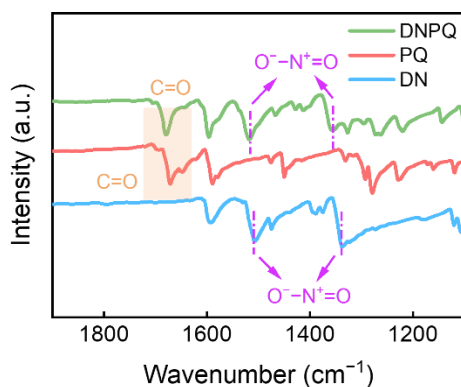
Fig. S1 FT-IR spectra of DNPQ, PQ and DN.

Notes to Fig. S1: FT-IR spectra indicate the presence of C=O groups at 1670 and 1679 cm^{-1} in PQ and DNPQ, as well as NO$_2$ groups at 1519 and 1359 cm^{-1} in DN and DNPQ. This suggest that DNPQ contains dual functional groups of C=O and NO$_2$.
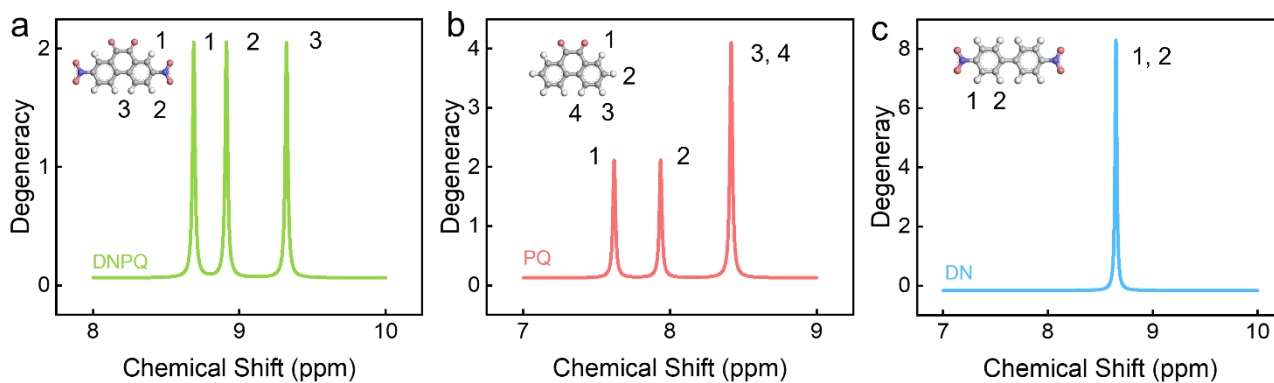
Fig. S2 H^1 NMR spectra of DNPQ, PQ and DN.
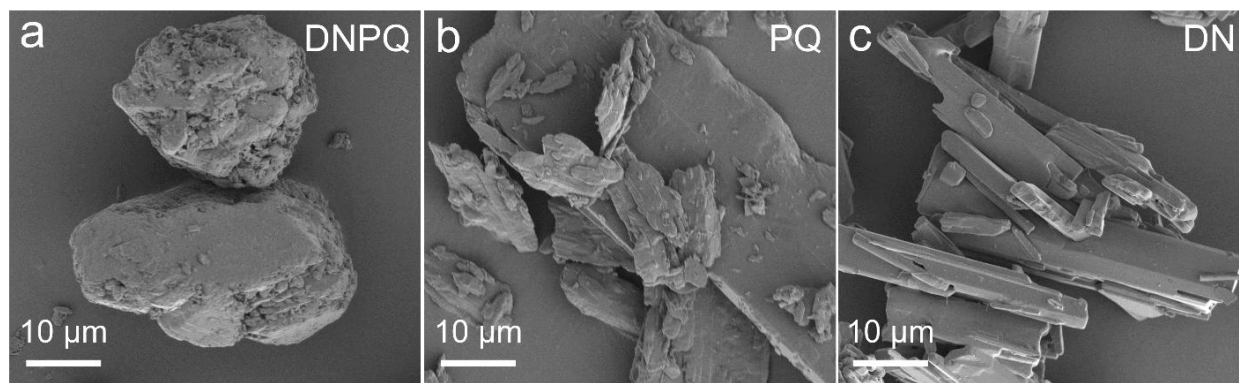
Fig. S3 SEM images of (a) DNPQ, (b) PQ, and (c) DN.
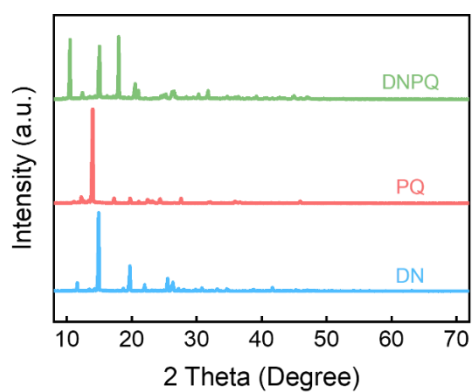
Fig. S4 XRD patterns of DNPQ, PQ and DN.
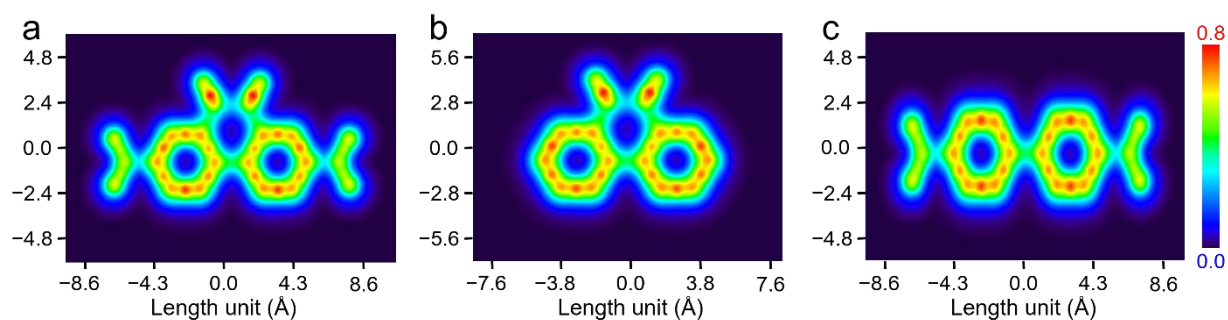
Fig. S5 The π-electron localized orbital locator map (LOL-π) of (a) DNPQ, (b) PQ and (c) DN molecules.
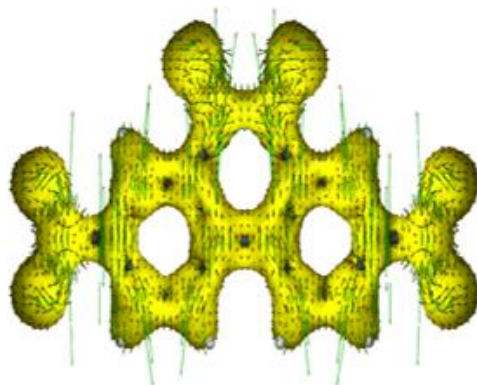
Fig. S6 ACID plots of DNPQ molecules.
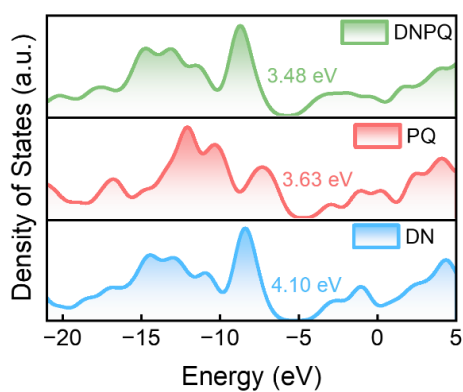
Fig. S7 Simulated projected density of states (DOS) of DNPQ, PQ and DN molecules.
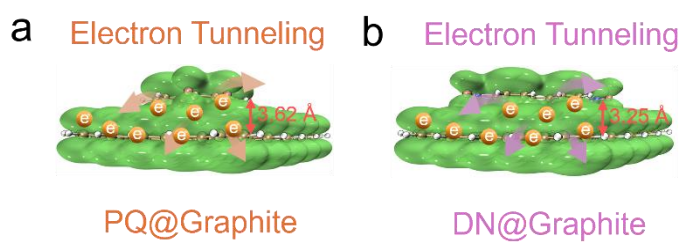
Fig. S8 The orbital analysis of (a) PQ and (b) DN molecules stacked on graphite skeleton for showing the interface electron transfer process.

Section S4. Electrochemical Results
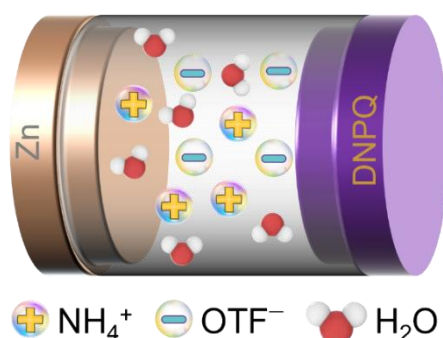
Fig. S9 Schematic configuration of Zn||DNPQ battery using aqueous NH₄OTF electrolyte.
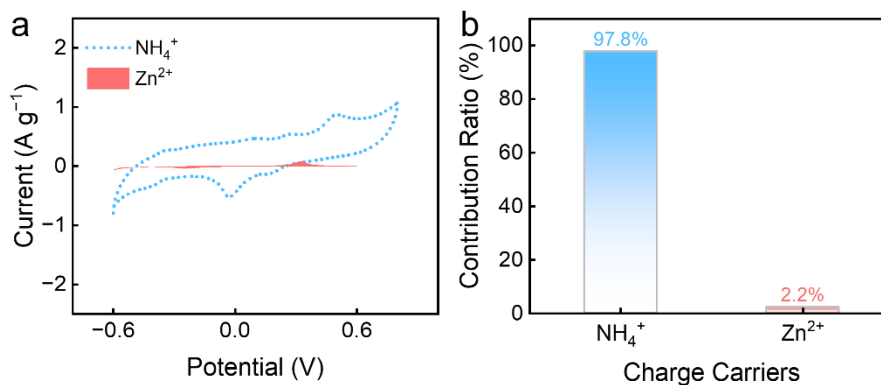
Fig. S10 (a) Three-electrode CV analysis (Pt wire as the counter electrode and graphite rod as the reference electrode) and (b) capacity contribution of NH_4^+ and Zn^{2+} ions.

Fig. S11 (a) Tested pH values and (b) ionic conductivities of two electrolytes. (c) GCD profile of DNPQ in two different electrolytes.
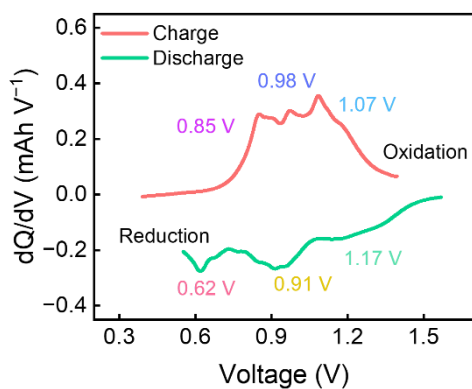
Fig. S12 Differential capacity profile.
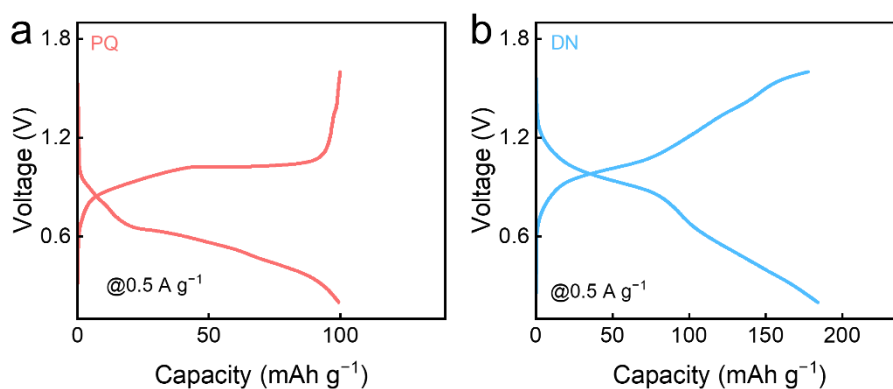
Fig. S13 GCD profiles of (a) PQ and (b) DN cathodes in NH$_4$OTF electrolyte.
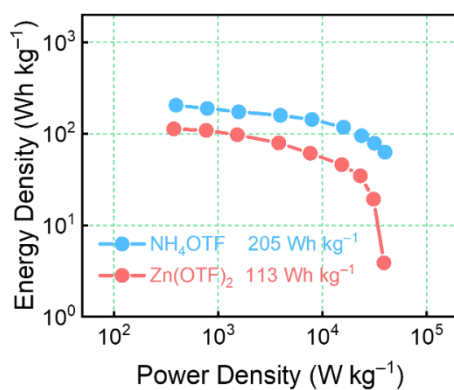
Fig. S14 Ragone plots of Zn||DNPQ batteries based on the mass loading of DNPQ in the cathode (5.1 mg cm^{-2}) using NH$_4$OTF and Zn(OTF)$_2$ electrolytes, respectively.

Fig. S15 (a) CV curves of DNPQ at 1−5 mV s^{-1}. (b) b values, and (c) capacitive contribution of Zn//DNPQ battery using NH$_4$OTF electrolyte.

Notes to Fig. S15: Plotting log*i* versus log*v* yields high power-exponent b values of 0.93−0.96 for the three redox peaks. It is well-established that a b-value is close to 0.5 means a diffusion-controlled process, while a b-value is close to 1 signifies a capacitive-controlled process in the charge storage mechanism. Almost 83% of the total stored charge is contributed by the surface redox reaction at 2 mV s^{-1}, along with the slight diffusion-limited process (17%).

Fig. S16 Capacity comparison of DNPQ with recently reported organics.

Fig. S17 (a, c) Voltage profiles and (b, d) Coulombic efficiency of Zn‖stainless-steel mesh cell in NH$_4$OTF and Zn(OTF)$_2$ electrolyte.

Fig. S18 Electrochemical impedance spectroscopy of pristine and cycled DNPQ cathode.
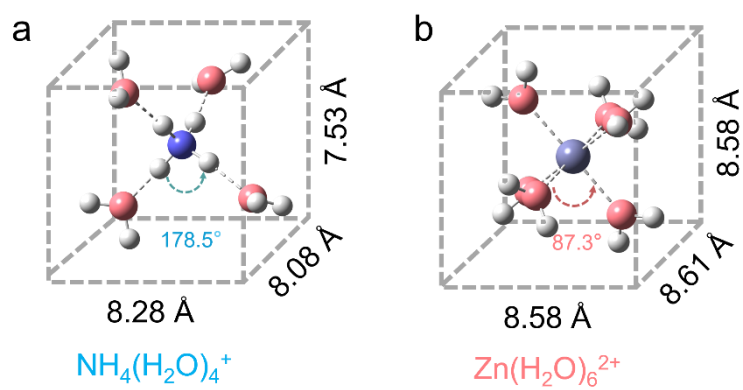
Fig. S19 Spatial geometric sizes of (a) hydrated NH_4^+ ions and (b) hydrated Zn^{2+} ions.
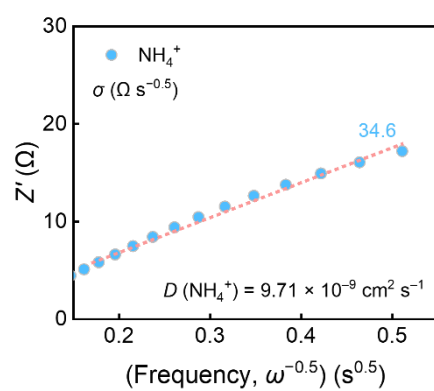
Fig. S20 Relationship between Z' and $\omega^{-0.5}$ in the intermediate frequency and corresponding NH_4^+ diffusion coefficient.

Fig. S21 Electrochemical impedance spectra of Zn‖DNPQ battery at different temperatures in (a) NH4OTF and (b) Zn(OTF)2 electrolytes, respectively. The equivalent circuit of Nyquist plots for DNPQ in (c) NH4OTF and (d) Zn(OTF)2 electrolytes, including the equivalent series resistances (R_s), the charge transfer resistance (R_{ct}), the contact angle element (CPE), and Warburg resistance (Z_w). (e) Estimated R_{ct} values.
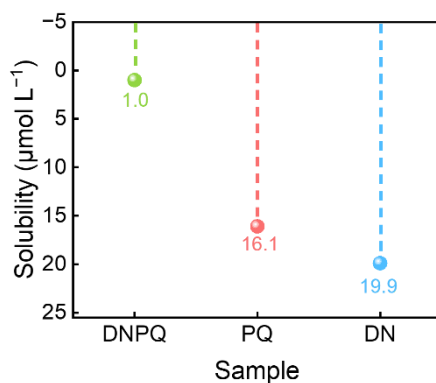
Fig. S22 Solubility of three samples.
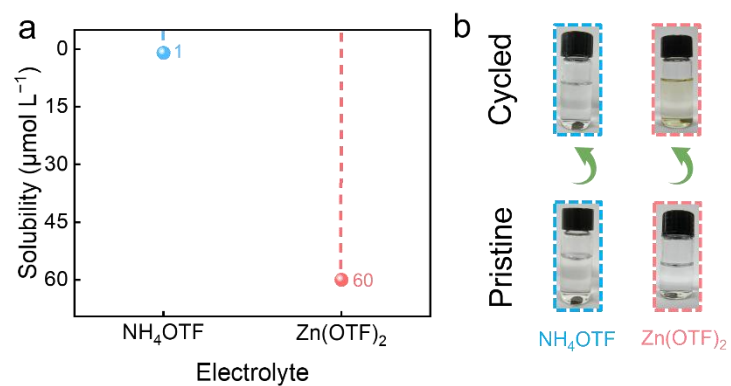
Fig. S23 (a) Solubility and (b) photographs of DNPQ in two electrolytes.
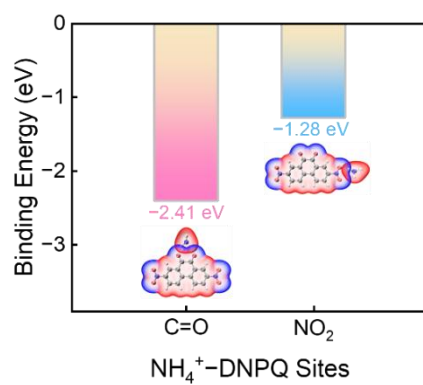
Fig. S24 NH_4^+ uptake energies of DNPQ with different sites.
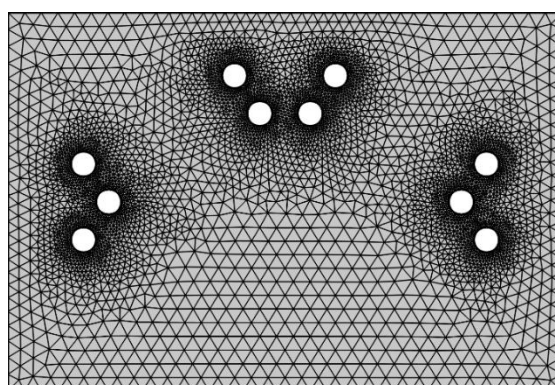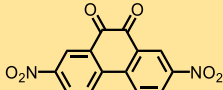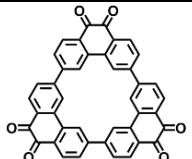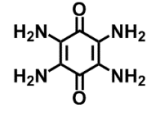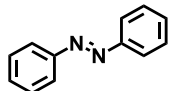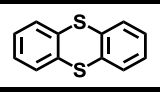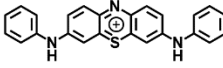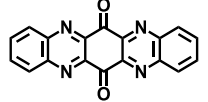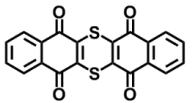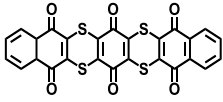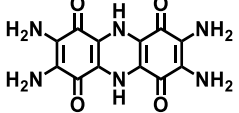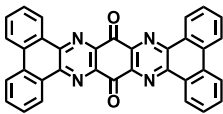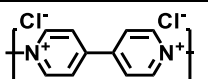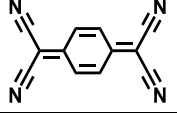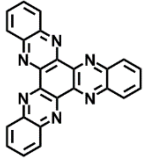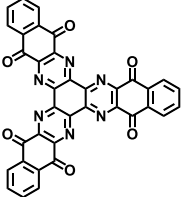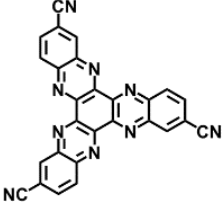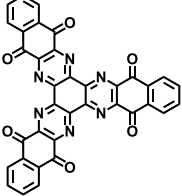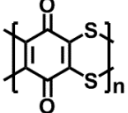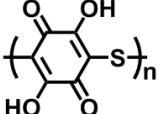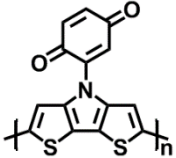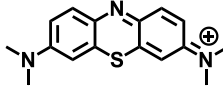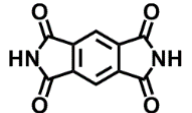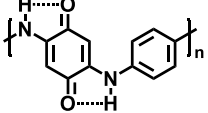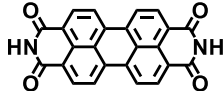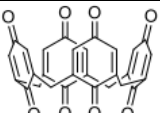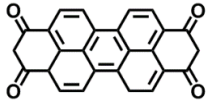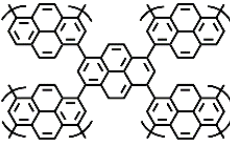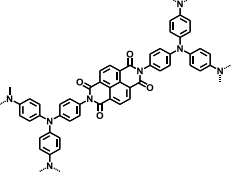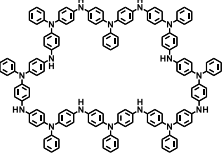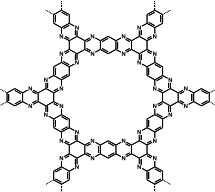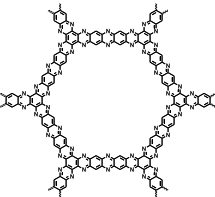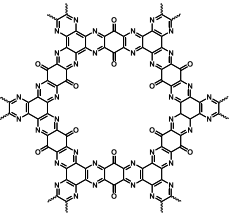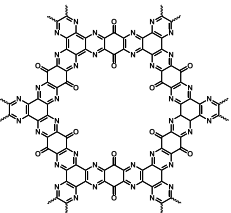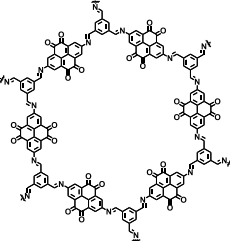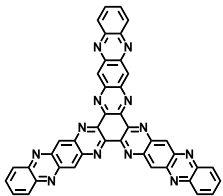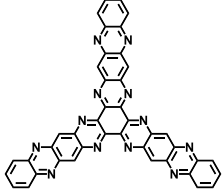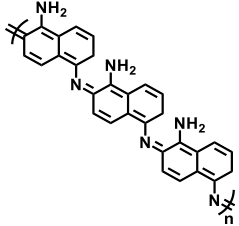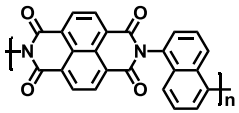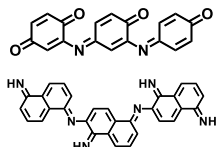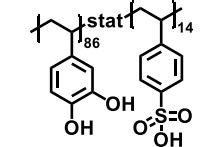
Fig. S25 The established geometry model of DNPQ.

Table S1 Comparison of rate capacity, energy density and cycling performance of recently reported organic cathode materials for ZOBs in the literatures.

Organic Structure	Rate Capacity (mAh g^{-1})	Energy Density (E, Wh kg^{-1})	Cycling Life Capacity Retention (%)	Refs.
	260@0.5 A g^{-1} 82@50 A g^{-1}	205	81.1%, 80,000 cycles, 20 A g^{-1}	This work
	210@0.15 A g^{-1}	N/A	99%, 500 cycles, 0.15 A g^{-1}	S29
	213@5 A g^{-1}	N/A	83%, 1000 cycles, 5 A g^{-1}	S30
	163@0.8 A g^{-1}	62.9	95%, 200 cycles, 5 A g^{-1}	S31
	66@20 A g^{-1}	67	82%, 8000 cycles, 1 A g^{-1}	S32
	48.9@30 A g^{-1}	116.8	82.5%, 4000 cycles, 1 A g^{-1}	S33
	182@2 A g^{-1}	282	92%, 250 cycles, 0.05 A g^{-1}	S34
	97@2 A g^{-1}	126.5	83.8%, 23,000 cycles, 2 A g^{-1}	S35
	120@10 A g^{-1}	N/A	65%, 58,000 cycles, 10 A g^{-1}	S36
	182@10 A g^{-1}	N/A	81.3%, 3000 cycles, 10 A g^{-1}	S37
	140.7@20 A g^{-1}	N/A	90.8%, 30,000 cycles, 5 A g^{-1}	S38
	82@20 A g^{-1}	68	70%, 45,000 cycles, 5 A g^{-1}	S39
	173@5 A g^{-1}	195	76%, 1000 cycles, 3 A g^{-1}	S40

	123@20 A g^{-1}	N/A	93.3%, 5000 cycles, 5 A g^{-1}	S41
	177.5@9 A g^{-1}	289	75%, 11,000 cycles, 5 A g^{-1}	S42
	190@20 A g^{-1}	149.3	91%, 5800 cycles, 5 A g^{-1}	S43
	145@20 A g^{-1}	N/A	82%, 1000 cycles, 10 A g^{-1}	S44
	176@10 A g^{-1}	190.1	75%, 10,000 cycles, 20 A g^{-1}	S45
	161@5 A g^{-1}	157.1	79%, 2000 cycles, 2 A g^{-1}	S46
	60@5 A g^{-1}	139	75%, 500 cycles, 2 A g^{-1}	S47
	58@83.5 A g^{-1}	N/A	86%, 20,000 cycles, 16.7 A g^{-1}	S48
	120@1C	N/A	93.5%, 1000 cycles, 1C	S49
	277@20 A g^{-1}	242	85%, 4800 cycles, 10 A g^{-1}	S50
	121@5 A g^{-1}	44	96%, 1500 cycles, 3 A g^{-1}	S51
	172@1 A g^{-1}	220	87%, 1000 cycles, 0.5 A g^{-1}	S52

	105@8 A g^{-1}	60	81%, 500 cycles, 8 A g^{-1}	S53
	105@3 A g^{-1}	N/A	96.4%, 38,000 cycles, 3 A g^{-1}	S54
	73@7 A g^{-1}	66.5	85%, 4000 cycles, 10 mV s^{-1}	S55
	107.5@6 A g^{-1}	236	87.6%, 1000 cycles, 6 A g^{-1}	S56
	200@10 A g^{-1}	N/A	91.2%, 9700 cycles, 10 A g^{-1}	S57
	68@10 A g^{-1}	N/A	62%, 10,000 cycles, 10 A g^{-1}	S58
	95.6@10 A g^{-1}	N/A	88%, 10,000 cycles, 5 A g^{-1}	S59
	37.5@10 A g^{-1}	N/A	100%, 7000 cycles, 6 A g^{-1}	S60
	108@500 A g^{-1}	92.4	98%, 10,000 cycles, 5 A g^{-1}	S61

	131@60 A g^{-1}	153.9	92.7%, 30,000 cycles, 30 A g^{-1}	S62
	100@20 A g^{-1}	43.1	100%, 13,000 cycles, 20 A g^{-1}	S63
	65@30 A g^{-1}	139.6	78%, 3000 cycles, 5 A g^{-1}	S64
	110.3@5 A g^{-1}	68.7	80.2%, 10,000 cycles, 5 A g^{-1}	S65
	132@40 A g^{-1}	N/A	90.1%, 5000 cycles, 5 A g^{-1}	S66
	98@141 A g^{-1}	352	83%, 48,000 cycles, 9.4 A g^{-1}	S67

References:

S1.   M. J. Frisch, G. W. Trucks, H. B. Schlegel, G. E. Scuseria, M. A. Robb, J. R. Cheeseman, G. Scalmani, V. Barone, G. A. Petersson, H. Nakatsuji, X. Li, M. Caricato, A. V. Marenich, J. Bloino, B. G. Janesko, R. Gomperts, B. Mennucci, H. P. Hratchian, J. V. Ortiz, A. F. Izmaylov, J. L. Sonnenberg, Williams, F. Ding, F. Lipparini, F. Egidi, J. Goings, B. Peng, A. Petrone, T. Henderson, D. Ranasinghe, V. G. Zakrzewski, J. Gao, N. Rega, G. Zheng, W. Liang, M. Hada, M. Ehara, K. Toyota, R. Fukuda, J. Hasegawa, M. Ishida, T. Nakajima, Y. Honda, O. Kitao, H. Nakai, T. Vreven, K. Throssell, J. A. Montgomery Jr., J. E. Peralta, F. Ogliaro, M. J. Bearpark, J. J. Heyd, E. N. Brothers, K. N. Kudin, V. N. Staroverov, T. A. Keith, R. Kobayashi, J. Normand, K. Raghavachari, A. P. Rendell, J. C. Burant, S. S. Iyengar, J. Tomasi, M. Cossi, J. M. Millam, M. Klene, C. Adamo, R. Cammi, J. W. Ochterski, R. L. Martin, K. Morokuma, O. Farkas, J. B. Foresman and D. J. Fox, *Gaussian 16 Rev. A.03*, 2016.

S2.   E. R. Johnson, S. Keinan, P. Mori-Sánchez, J. Contreras-García, A. J. Cohen and W. Yang, *J. Am. Chem. Soc.*, 2010, **132**, 6498−6506.

S3.   T. Lu and F. Chen, *J. Comput. Chem.*, 2012, **33**, 580−592.

S4.   T. Lu, *J. Chem. Phys.*, 2024, **161**, 082503.

S5.   G. Kresse and J. Furthmüller, *Comput. Mater. Sci.*, 1996, **6**, 15−50.

S6.   P. E. Blöchl, *Phys. Rev. B*, 1994, **50**, 17953−17979.

S7.   J. P. Perdew, K. Burke and M. Ernzerhof, *Phys. Rev. Lett.*, 1996, **77**, 3865−3868.

S8.   N. Zhang, A. Jalil, D. Wu, S. Chen, Y. Liu, C. Gao, W. Ye, Z. Qi, H. Ju, C. Wang, X. Wu, L. Song, J. Zhu and Y. Xiong, *J. Am. Chem. Soc.*, 2018, **140**, 9434−9443.

S9.   L. Martínez, R. Andrade, E. G. Birgin and J. M. Martínez, *J. Comput. Chem.*, 2009, **30**, 2157−2164.

S10.   M. J. Abraham, T. Murtola, R. Schulz, S. Páll, J. C. Smith, B. Hess and E. Lindahl, *SoftwareX*, 2015, **1−2**, 19−25.

S11.   S. Páll, M. J. Abraham, C. Kutzner, B. Hess and E. Lindahl, Cham, 2015.

S12.   B. Hess, C. Kutzner, D. van der Spoel and E. Lindahl, *J. Chem. Theor. Comput.*, 2008, **4**, 435−447.

S13.   S. Pronk, S. Páll, R. Schulz, P. Larsson, P. Bjelkmar, R. Apostolov, M. R. Shirts, J. C. Smith,

P. M. Kasson, D. van der Spoel, B. Hess and E. Lindahl, *Bioinformatics*, 2013, **29**, 845−854.

S14.   W. L. Jorgensen, D. S. Maxwell and J. Tirado-Rives, *J. Am. Chem. Soc.*, 1996, **118**, 11225−11236.

S15.   H. J. C. Berendsen, J. R. Grigera and T. P. Straatsma, *J. Phys. Chem.*, 1987, **91**, 6269–6271.

S16.   B. Hess, H. Bekker, H. J. C. Berendsen and J. G. E. M. Fraaije, *J. Comput. Chem.*, 1997, **18**, 1463−1472.

S17.   G. Bussi, D. Donadio and M. Parrinello, *J. Chem. Phys.*, 2007, **126**, 014101.

S18.   U. Essmann, L. Perera, M. L. Berkowitz, T. Darden, H. Lee and L. G. Pedersen, *J. Chem. Phys.* , 1995, **103**, 8577−8593.

S19.   W. Humphrey, A. Dalke and K. Schulten, *J. Mol. Graph.*, 1996, **14**, 33−38.

S20.   W. Kohn and L. J. Sham, *Phys. Rev.*, 1965, **140**, A1133−A1138.

S21.   M. Liu, Y. Pang, B. Zhang, P. De Luna, O. Voznyy, J. Xu, X. Zheng, C. T. Dinh, F. Fan, C. Cao, F. P. G. de Arquer, T. S. Safaei, A. Mepham, A. Klinkova, E. Kumacheva, T. Filleter, D. Sinton, S. O. Kelley and E. H. Sargent, *Nature*, 2016, **537**, 382−386.

S22.   L. Xiang, S. Yuan, F. Wang, Z. Xu, X. Li, F. Tian, L. Wu, W. Yu and Y. Mai, *J. Am. Chem. Soc.*, 2022, **144**, 15497−15508.

S23.   C. Xie, X. Hu, Z. Guan, X. Li, F. Zhao, Y. Song, Y. Li, X. Li, N. Wang and C. Huang, *Angew. Chem. Int. Ed.* , 2020, **59**, 13542−13546.

S24.   B. Liu, X. Hao, T. Zhai, S. Sun, H. Zhang, P. A. Koudakan, C. Wei, G. Wang and H. Xia, *Energy Storage Mater.*, 2022, **48**, 403−411.

S25.   N. Wang, R. Zhou, H. Li, Z. Zheng, W. Song, T. Xin, M. Hu and J. Liu, *ACS Energy Lett.*, 2021, **6**, 1141−1147.

S26.   F. Ye, Q. Liu, H. Dong, K. Guan, Z. Chen, N. Ju and L. Hu, *Angew. Chem. Int. Ed.* , 2022, **61**, e202214244.

S27.   H. Peng, S. Huang, V. Montes-García, D. Pakulski, H. Guo, F. Richard, X. Zhuang, P. Samorì and A. Ciesielski, *Angew. Chem. Int. Ed.*, 2023, **62**, e202216136.

S28.   Y. Lu, X. Hou, L. Miao, L. Li, R. Shi, L. Liu and J. Chen, *Angew. Chem. Int. Ed.*, 2019, **58**, 7020−7024.

S29.   K. W. Nam, H. Kim, Y. Beldjoudi, T.-w. Kwon, D. J. Kim and J. F. Stoddart, *J. Am. Chem. Soc.*, 2020, **142**, 2541−2548.

S30. Z. Lin, H.-Y. Shi, L. Lin, X. Yang, W. Wu and X. Sun, *Nat. Commun.*, 2021, **12**, 4424.

S31. Y. Chen, H. Dai, K. Fan, G. Zhang, M. Tang, Y. Gao, C. Zhang, L. Guan, M. Mao, H. Liu, T. Zhai and C. Wang, *Angew. Chem. In. Ed.*, 2023, **62**, e202302539.

S32. H. Cui, T. Wang, Z. Huang, G. Liang, Z. Chen, A. Chen, D. Wang, Q. Yang, H. Hong, J. Fan and C. Zhi, *Angew. Chem. Int. Ed.*, 2022, **61**, e202203453.

S33. N. Wang, Z. Guo, Z. Ni, J. Xu, X. Qiu, J. Ma, P. Wei and Y. Wang, *Angew. Chem. Int. Ed.*, 2021, **60**, 20826−20832.

S34. Y. Gao, G. Li, F. Wang, J. Chu, P. Yu, B. Wang, H. Zhan and Z. Song, *Energy Storage Mater.*, 2021, **40**, 31−40.

S35. Y. Wang, C. Wang, Z. Ni, Y. Gu, B. Wang, Z. Guo, Z. Wang, D. Bin, J. Ma and Y. Wang, *Adv. Mater.*, 2020, **32**, 2000338.

S36. Q.-Q. Sun, T. Sun, J.-Y. Du, K. Li, H.-M. Xie, G. Huang and X.-B. Zhang, *Adv. Mater.*, 2023, **35**, 2301088.

S37. L. Lin, Z. Lin, J. Zhu, K. Wang, W. Wu, T. Qiu and X. Sun, *Energy Environ. Sci.*, 2023, **16**, 89−96.

S38. T. Sun, W. Zhang, Z. Zha, M. Cheng, D. Li and Z. Tao, *Energy Storage Mater.*, 2023, **59**, 102778.

S39. L. Xie, K. Xu, W. Sun, Y. Fan, J. Zhang, Y. Zhang, H. Zhang, J. Chen, Y. Shen, F. Fu, H. Kong, G. Wu, J. Wu, L. Chen and H. Chen, *Angew. Chem. Int. Ed.*, 2023, **62**, e202300372.

S40. Y. Zhong, Y. Li, J. Meng, X. Lin, Z. Huang, Y. Shen and Y. Huang, *Energy Storage Mater.*, 2021, **43**, 492−498.

S41. Z. Tie, L. Liu, S. Deng, D. Zhao and Z. Niu, *Angew. Chem. Int. Ed.*, 2020, **59**, 4920−4924.

S42. Y. Chen, J. Li, Q. Zhu, K. Fan, Y. Cao, G. Zhang, C. Zhang, Y. Gao, J. Zou, T. Zhai and C. Wang, *Angew. Chem. Int. Ed.*, 2022, **61**, e202116289.

S43. Z. Ye, S. Xie, Z. Cao, L. Wang, D. Xu, H. Zhang, J. Matz, P. Dong, H. Fang, J. Shen and M. Ye, *Energy Storage Mater.*, 2021, **37**, 378−386.

S44. Z. Tie, Y. Zhang, J. Zhu, S. Bi and Z. Niu, *J. Am. Chem. Soc.*, 2022, **144**, 10301−10308.

S45. J. Xie, F. Yu, J. Zhao, W. Guo, H.-L. Zhang, G. Cui and Q. Zhang, *Energy Storage Mater.*, 2020, **33**, 283−289.

S46. T. Sun, Z.-J. Li, Y.-F. Zhi, Y.-J. Huang, H. J. Fan and Q. Zhang, *Adv. Funct. Mater.*, 2021,

31, 2010049.

S47.   X. Wang, J. Xiao and W. Tang, *Adv. Funct. Mater.*, 2022, **32**, 2108225.

S48.   M. Tang, Q. Zhu, P. Hu, L. Jiang, R. Liu, J. Wang, L. Cheng, X. Zhang, W. Chen and H. Wang, *Adv. Funct. Mater.*, 2021, **31**, 2102011.

S49.   M. Na, Y. Oh and H. R. Byon, *Chem. Mater.*, 2020, **32**, 6990−6997.

S50.   H. Zhang, D. Xu, L. Wang, Z. Ye, B. Chen, L. Pei, Z. Wang, Z. Cao, J. Shen and M. Ye, *Small*, 2021, **17**, 2100902.

S51.   N. Liu, X. Wu, Y. Zhang, Y. Yin, C. Sun, Y. Mao, L. Fan and N. Zhang, *Adv. Sci.*, 2020, **7**, 2000146.

S52.   Q. Zhao, W. Huang, Z. Luo, L. Liu, Y. Lu, Y. Li, L. Li, J. Hu, H. Ma and J. Chen, *Sci. Adv.*, 2018, **4**, eaao1761.

S53.   H. Zhang, Y. Fang, F. Yang, X. Liu and X. Lu, *Energy Environ. Sci.*, 2020, **13**, 2515−2523.

S54.   M. Yu, N. Chandrasekhar, R. K. M. Raghupathy, K. H. Ly, H. Zhang, E. Dmitrieva, C. Liang, X. Lu, T. D. Kühne, H. Mirhosseini, I. M. Weidinger and X. Feng, *J. Am. Chem. Soc.*, 2020, **142**, 19570−19578.

S55.   H. Zhang, L. Zhong, J. Xie, F. Yang, X. Liu and X. Lu, *Adv. Mater.*, 2021, **33**, 2101857.

S56.   Z. Li, J. Tan, X. Zhu, S. Xie, H. Fang, M. Ye and J. Shen, *Energy Storage Mater.*, 2022, **51**, 294−305.

S57.   W. Wang, V. S. Kale, Z. Cao, S. Kandambeth, W. Zhang, J. Ming, P. T. Parvatkar, E. Abou-Hamad, O. Shekhah, L. Cavallo, M. Eddaoudi and H. N. Alshareef, *ACS Energy Lett.*, 2020, **5**, 2256−2264.

S58.   W. Wang, V. S. Kale, Z. Cao, Y. Lei, S. Kandambeth, G. Zou, Y. Zhu, E. Abouhamad, O. Shekhah, L. Cavallo, M. Eddaoudi and H. N. Alshareef, *Adv. Mater.*, 2021, **33**, 2103617.

S59.   Z. Tian, V. S. Kale, Y. Wang, S. Kandambeth, J. Czaban-Jóźwiak, O. Shekhah, M. Eddaoudi and H. N. Alshareef, *J. Am. Chem. Soc.*, 2021, **143**, 19178−19186.

S60.   S. Zheng, D. Shi, D. Yan, Q. Wang, T. Sun, T. Ma, L. Li, D. He, Z. Tao and J. Chen, *Angew. Chem. Int. Ed.*, 2022, **61**, e202117511.

S61.   C. Zhang, W. Ma, C. Han, L.-W. Luo, A. Daniyar, S. Xiang, X. Wu, X. Ji and J.-X. Jiang, *Energy Environ. Sci.*, 2021, **14**, 462−472.

S62.   S. Li, J. Shang, M. Li, M. Xu, F. Zeng, H. Yin, Y. Tang, C. Han and H.-M. Cheng, *Adv.*

Mater., 2023, **35**, 2207115.

S63.   J. Yang, H. Hua, H. Yang, P. Lai, M. Zhang, Z. Lv, Z. Wen, C. C. Li, J. Zhao and Y. Yang, *Adv. Energy Mater.*, 2023, **13**, 2204005.

S64.   L. Yan, Y. Zhang, Z. Ni, Y. Zhang, J. Xu, T. Kong, J. Huang, W. Li, J. Ma and Y. Wang, *J. Am. Chem. Soc.*, 2021, **143**, 15369−15377.

S65.   S. Zhang, K. Zhu, Y. Gao and D. Cao, *ACS Energy Lett.*, 2023, **8**, 889−897.

S66.   Y. Zhao, Y. Huang, F. Wu, R. Chen and L. Li, *Adv. Mater.*, 2021, **33**, 2106469.

S67.   N. Patil, C. Cruz, D. Ciurduc, A. Mavrandonakis, J. Palma and R. Marcilla, *Adv. Energy Mater.*, 2021, **11**, 2100939.